Electrochemical Properties of Submicron-Sized Li[Ni$_{1/3}$Co$_{1/3}$Mn$_{1/3}$]O$_2$ Cathode Materials for Lithium-Ion Battery

Hai-Bo Ren[1]*, Xiang-Yun Liu*[1]*, Hai-Peng Zhao*[1]* , Zheng-He Peng*[2,*]* and Yun-Hong Zhou*[2]

[1] Department of Chemistry and Chemical Engineering, Henan University of Urban Construction, Pingdingshan, 467044, P.R. China
[2] Department of Chemistry, Wuhan University, Wuhan, 430072, P.R. China
[*]E-mail: Zhhpeng@126.com

Li[Ni$_{1/3}$Co$_{1/3}$Mn$_{1/3}$]O$_2$ cathode material is synthesized via a simple solvent evaporation method. The SEM image shows that the particles of layered Li[Ni$_{1/3}$Co$_{1/3}$Mn$_{1/3}$]O$_2$ material is submicron in size. The electrochemical properties of Li[Ni$_{1/3}$Co$_{1/3}$Mn$_{1/3}$]O$_2$ materials are carried out by charge-discharge cycling test and the electrochemical reactions in the process of charge and discharge are also investigated by the cyclic voltammetry (CV). It is found that submicron-sized Li[Ni$_{1/3}$Co$_{1/3}$Mn$_{1/3}$]O$_2$ material has batter electrochemical performance, which delivers the higher initial discharge capacities of 209.6 mAhg^{-1} (2.7 ~ 4.6 V, 20 mAg^{-1}) with excellent cyclic performance.

1. INTRODUCTION

The lithium-ion secondary batteries with high energy density and power capability are extensively used as electrochemical power sources in a lot of modern equipments, such as mobile telephones, laptop computers, video-cameras and so on [1-5]. Among the lithium-ion secondary battery materials, manganese based layer-structured material Li[Ni$_{1/3}$Co$_{1/3}$Mn$_{1/3}$]O$_2$, which holds good electrochemical performance and safety characteristic, is considered to be one of the most promising battery materials.

To synthesize homogeneous Li[Ni$_{1/3}$Co$_{1/3}$Mn$_{1/3}$]O$_2$, different synthetic methods have been adopted [6-9], one of which is metal acetate decomposition .The metal acetate decomposition is one of solid state reaction methods by which one can prepare cathode materials for Lithium-ion batteries [10].

However, K.M. Shaju and P.G. Bruce [11] pointed out that the attempt to synthesize the material directly by commonly used solid state often results in an inhomogeneous impure product with lower capacity and poor cycling performance [12-15]. In the present work, $Li[Ni_{1/3}Co_{1/3}Mn_{1/3}]O_2$ was prepared by solvent evaporation method, which has the advantage of overcoming the above shortcomings when solid state raw materials were directly used to synthesize the product, and its structural, morphological and electrochemical behaviors were also characterized.

2. EXPERIMENTAL

2.1. Synthesis of $Li[Ni_{1/3}Co_{1/3}Mn_{1/3}]O_2$

Submicron-sized $Li[Ni_{1/3}Co_{1/3}Mn_{1/3}]O_2$ cathode materials are synthesized by a solvent evaporation method. $LiC_2H_3O_2 \cdot 2H_2O$, $Ni(C_2H_3O_2)_2 \cdot 4H_2O$, $Co(C_2H_3O_2)_2 \cdot 4H_2O$ and $Mn(C_2H_3O_2)_2 \cdot 4H_2O$ were used as the starting materials in quantities corresponding to 0.02mol stoichiometric $Li[Ni_{1/3}Co_{1/3}Mn_{1/3}]O_2$ with 6% excess of Li, which is adopted to make up the loss of lithium in sintering process and it is an appropriate quantity based on our former work [9]. These reagents were dissolved into a proper amount of distilled water and a mauve solution was obtained. The resulting solution was first heated at 100 ˚C with magnetic stirring until viscous, and then dried at 120 ˚C for 12h to obtain a mixed precursor. The mixed precursor was pre-heated at 500˚C for 6h and finally calcined at different temperatures to take submicron-sized $Li[Ni_{1/3}Co_{1/3}Mn_{1/3}]O_2$.

Contrasted with this method, $Li[Ni_{1/3}Co_{1/3}Mn_{1/3}]O_2$ was also carried out by a solid state method in this work. The starting materials and proportion were the same as those of the solvent evaporation method. All procedures were carried out in air.

2.2. Measurements

Thermogravimetric (TG) and differential scanning calorimeter (DSC) for the mixture was carried out with a Netzsch STA 449C instrument to determine approximate calcining temperature and procedure. The mixture sample was heated at 10 ˚C min^{-1} from room temperature to 800 ˚C in a static air atmosphere.

X-ray diffraction measurements of the $Li[Ni_{1/3}Co_{1/3}Mn_{1/3}]O_2$ materials were carried out using X-ray diffraction (Shimadzu XRD-6000) with Cu *Kα* radiation (λ=1.54056Å). Analysis of structural properties was performed with FullProf program [16]. Particle morphology of the powders after calcination was observed under a scanning electron microscope (SEM, QUANTA-200).

Electrochemical charge-discharge experiments were performed with the CR2016 coin-type cell. Test cathode electrodes were prepared by mix 80:15:5 (mass ratio) of active material, acetylene black and PTFE binder, respectively, in isopropyl alcohol. The test cells were assembled with the electrode prepared above as cathode, lithium metal as anode, and Celgard 2300 film as separator in an argon-filled glove box. The electrolyte was 1M $LiPF_6$ dissolved in EC+DMC (1:1 volume ratio).

Cyclic voltammetry (CV) experiments were carried out at a scanning rate $0.1 mVs^{-1}$ between 2.8 and 4.8V versus Li/Li$^+$.

3. RESULTS AND DISCUSSION

3.1. Thermal properties

TG and DSC are used to investigate the reaction process during the heat treatment of the dried powder. Figure 1 shows the TG/DSC curves of the mixed precursor.
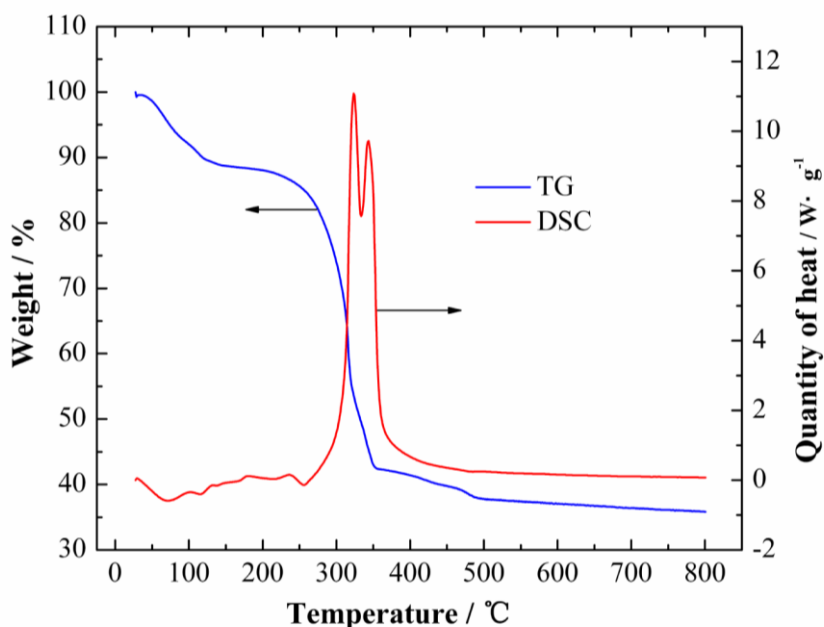

Figure 1. TG/DSC curves of the powder after being dried at 120 ˚C for 12h.

It is found that there is little water left in the precursor after being dried at 120 ˚C for 12 h, but the precursor could absorb some water from air before TG/DSC experiments. Therefore, the loss of weight from room temperature to 120 ˚C should be assigned to the evaporation of the absorbed water with a corresponding small broad endothermic peak on DSC curve. The weight loss at the temperature between 210 ˚C and 500 ˚C is associated with the decomposition of the acetates, which results in the formation of final Li[Ni$_{1/3}$Co$_{1/3}$Mn$_{1/3}$]O$_2$. The 52.12 wt. % of weight loss in this range determined by TG experiment agrees with the value of 53.87 wt. % that is calculated from the dehydration of the acetates without crystal water. It can be clearly seen that the weight loss is almost zero above 500˚C, which indicates that material will completely form above this temperature. Therefore, 800˚C, 850˚C, 900˚C, 950 ˚C are selected as the calcining temperatures.

3.2. Structure analysis

Figure 2 shows the XRD patterns for the samples prepared by a solvent evaporation method at calcination temperatures of 800 ˚C, 850 ˚C, 900 ˚C, 950 ˚C for 20h, respectively.
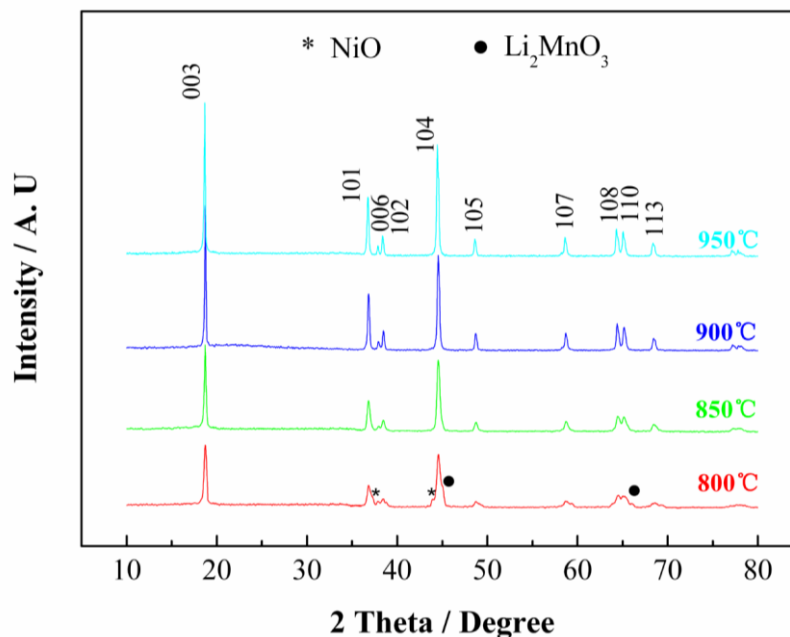

Figure 2. X-ray diffraction patterns of Li[Ni$_{1/3}$Co$_{1/3}$Mn$_{1/3}$]O$_2$ samples prepared by a solvent evaporation method at different temperatures for 20h.

It can be seen from Figure 2 that the XRD patterns of the materials at 850 ˚C, 900 ˚C and 950 ˚C can be indexed by a hexagonal α-NaFeO$_2$ structure (space group: $R\bar{3}m$) without any impurity peaks. Identified carefully, the trace amounts of impurity, NiO and Li$_2$MnO$_3$, are observed in the sample at 800 ˚C, as marked in figure. Therefore, a single phase Li[Ni$_{1/3}$Co$_{1/3}$Mn$_{1/3}$]O$_2$ compound can be prepared above 800 ˚C. Lattice parameters of the materials are supplied in Table 1.

Table 1. Lattice parameters of Li[Ni$_{1/3}$Co$_{1/3}$Mn$_{1/3}$]O$_2$ samples prepared at different conditions.

Temperatures	a (Å)	c (Å)	c/a	V (Å^3)	$I_{(003)}/I_{(104)}$
850 ˚C	2.8618	14.2359	4.9744	100.97	1.21
900 ˚C (SEP)	2.8635	14.2448	4.9746	101.15	1.49
950 ˚C	2.8644	14.2498	4.9748	101.25	1.36
900 ˚C (SSP)	2.8579	14.2042	4. 9702	100.47	1.33

According to Table 1, with increasing calcination temperature from 850 ˚C to 950 ˚C, the lattice parameter, *a*, which is related to average metal-metal intra-slab distance, *c*, correlated to the average metal-metal inter-slab distance, and the cell volume *V* all increase while the trigonal distortion, *c/a*, which indicates hexagonal structure disorder [17], is virtually unchanged. These results show that the hexagonal ordering does not change with calcinations temperature increasing. Meanwhile, it can also be seen clearly from Figure 2 that the patterns of the materials at 800 ˚C and 850 ˚C show some broader diffraction peaks, which indicates that the material doesn't crystallize very well. For the materials at 900 ˚C and 950 ˚C, the narrowness of the diffraction lines indicates a good crystallinity and suggests a homogeneous distribution of the cations within the structure at higher temperatures. Therefore, with calcinations temperature increasing, the full width at half maximum is getting smaller, which means that firing at much higher temperature brings about improved crystallinity [18]. In addition, the crystallite sizes calculated by procedure are 27.62, 33.45, 36.85 and 41.32 nm for the materials at 800 ˚C, 850 ˚C, 900 ˚C, 950 ˚C, respectively. It is very obvious that the crystallite sizes increase with calcination temperature increasing. In the XRD pattern, the integrated peak splits of (006)/(102) and (108)/(110) doublets are regarded as an indicator of characteristics of layered structure materials [19, 20]. According to Figure 2, the (006) and (102) peaks and (108) and (110) peaks are clearly split above 800˚C, especially for the materials at 900 ˚C and 950 ˚C, which reveals that the ideal layered structure should exist in the materials at 900 ˚C and 950 ˚C. Hwang et al. [21] believed that the intensity ratio of the (003) and (104) peaks ($I_{(003)}/I_{(104)}$) could be used to identify the cation mixing degree. Generally, when the value of intensity ratio is more than 1.2, the cation mixing is smaller with good layered structure and the higher value indicates lower cation mixing. The $I_{(003)}/I_{(104)}$ values of the samples are also presented in Table 1.
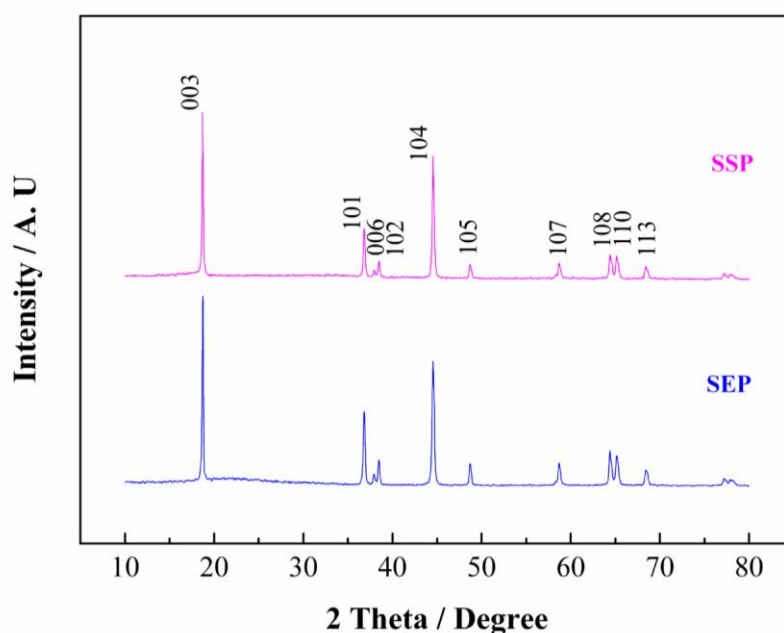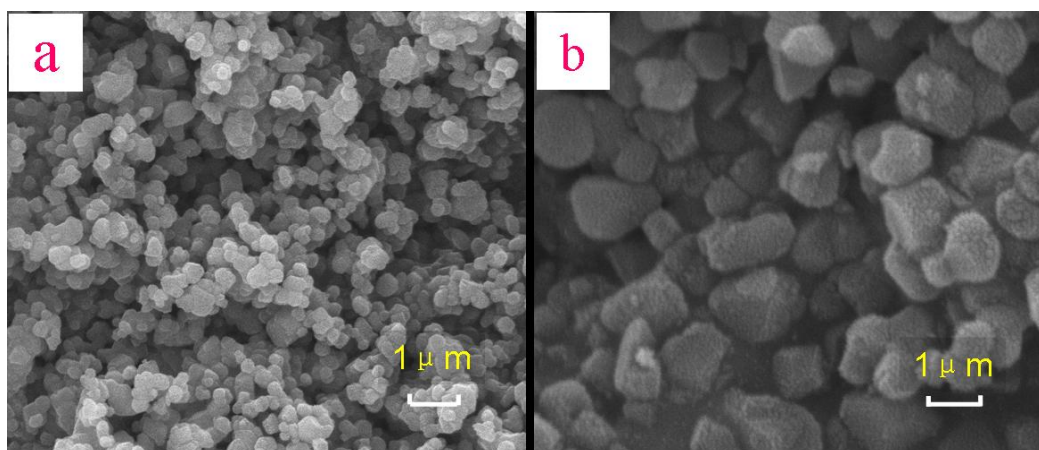

Figure 3. XRD patterns of Li[Ni$_{1/3}$Co$_{1/3}$Mn$_{1/3}$]O$_2$ prepared by different methods.

From Table 1, the sample at 900 ˚C holds more excellent structural integrity (bigger $I_{(003)}/I_{(104)}$), i.e. lower cation mixing than that at other temperatures. Based on the above results, it is suggested that Li[Ni$_{1/3}$Co$_{1/3}$Mn$_{1/3}$]O$_2$ materials calcined at 900 ˚C for 20h should display distinct electrochemical performances. Therefore, we will mainly focus on the samples synthesized at 900 ˚C for 20h in the following discussions.

The influences of synthetic methods on the crystal structure are also shown in Figure 3 and Table 1. From Figure 3, The XRD patterns of the sample prepared at 900 ˚C for 20h by a solvent evaporation method (denoted as SEP) present sharper peaks than that synthesized at 900 ˚C for 20h by a solid state method (denoted as SSP), which indicates that SEP holds higher crystallinity than SSP. From Table 1, the lattice parameters *a* and *c* for SEP is 2.8635 Å and 14.2448 Å, respectively, while *a* and *c* for SSP is 2.8579 Å and 14.2042 Å, respectively. It is clear that *c/a* for SSP is smaller than that for SEP, which shows SSP holds poorer hexagonal structure disorder [17]. In addition, the $I_{(003)}/I_{(104)}$ value of the sample for SEP is bigger than that for SSP, so we can draw the conclusion that the sample for SEP has better structural integrity than that for SSP.

3.3. Morphology of the particles

SEM micrographs of the two samples of Li[Ni$_{1/3}$Co$_{1/3}$Mn$_{1/3}$]O$_2$ (SEP and SSP) are illustrated in Figure 4. SSP powder consists of grains of average 1μm with no characteristic morphology. The morphology of SEP, however, is obviously different from that of SSP. SEP powder is composed of ball-like shape with an average diameter of about 300nm. It is obvious that the specific surface area of SEP particles is bigger than that of SSP.


Figure 4. SEM micrographs of Li[Ni$_{1/3}$Co$_{1/3}$Mn$_{1/3}$]O$_2$ prepared by different methods. (a) SEP; (b) SSP

As is well known, the influence of particle size, morphology and surface area to the battery performance is of great importance. We believe that differences of SEP and SSP in size, morphology and surface area should result in differences in their electrochemical performance.

3.4. Electrochemical characterization

The electrochemical properties of Li[Ni$_{1/3}$Co$_{1/3}$Mn$_{1/3}$]O$_2$ samples are strongly affected by the synthetic methods. Figure 5 shows the cyclic voltammetry curves of SEP and SSP samples.
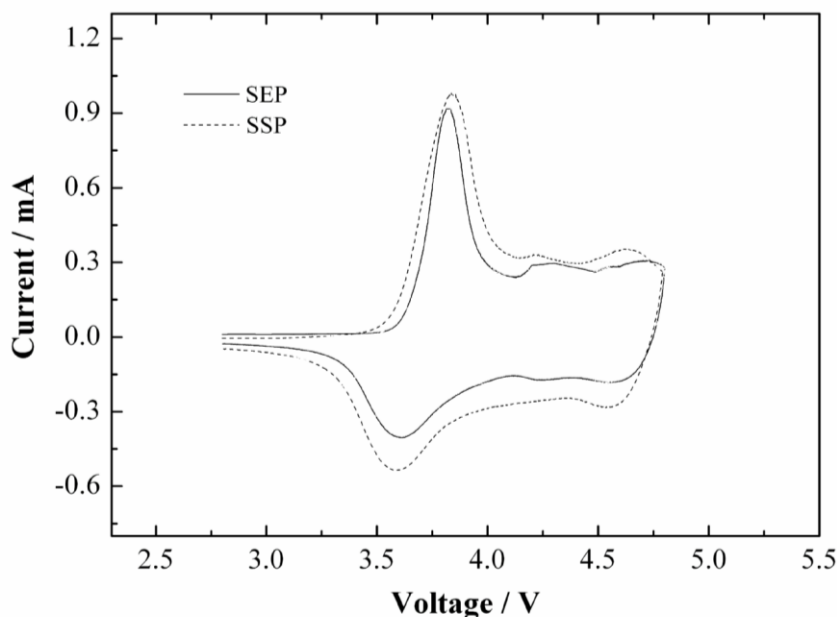
Figure 5. CV curves of Li[Ni$_{1/3}$Co$_{1/3}$Mn$_{1/3}$]O$_2$ samples operated from 2.8 ~ 4.8 V at a scan rate of 0.1mVs^{-1}.

As shown in Figure 5, the two samples show the two anodic peaks at 3.8 ~ 3.9 V and 4.6 ~ 4.8 V whereas the corresponding cathodic peak is at 3.5 ~ 3.6 V and 4.5 ~ 4.6 V. They are ascribed to Ni^{2+}/Ni^{4+} and Co^{3+}/Co^{4+} redox couples [7]. The major oxidation peak voltage for SEP, 3.84 V, shifts to the higher one for SSP, 3.91V. It implies that the polarization of SSP is bigger than that of SEP, which is probably attributed to the increased resistance inside the battery with respect to specific surface area because SSP particle has smaller specific surface area with bigger particle size shown in Figure 4. The redox current peaks correspond with the intercalation reaction of lithium ion in the layered Li[Ni$_{1/3}$Co$_{1/3}$Mn$_{1/3}$]O$_2$,

$$Li[Ni_{1/3}Co_{1/3}Mn_{1/3}]O_2 = Li_{1-x}[Ni_{1/3}Co_{1/3}Mn_{1/3}]O_2 + xLi^+ + xe^- \quad (1)$$
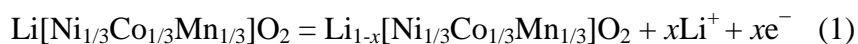
where $x < 1$. The theoretical discharge capacity ($x = 1$) is 278 mAhg^{-1}.

Figure 6 and Figure 7 show the initial charge-discharge curves and cycling performances of SEP and SSP, respectively. The cell was cycled between 3.0 and 4.3 V at room temperature at a current density of 20 mAg^{-1} (0.1 C), here the C-rate was calculated with 200 mAhg^{-1} as a theoretical capacity. It is clear that synthetic methods have a big effect on initial charge and discharge capacities.

According to Figure 6, the highest initial discharge capacity of 168.5 mAhg^{-1} and the lowest irreversible capacity of 13.6% are obtained from SEP. It is comparable or somewhat higher than that of

the reported [18, 22]. However, SSP delivers 154.9 mAhg^{-1} as initial discharge capacity and shows irreversible capacity of 14.8%.
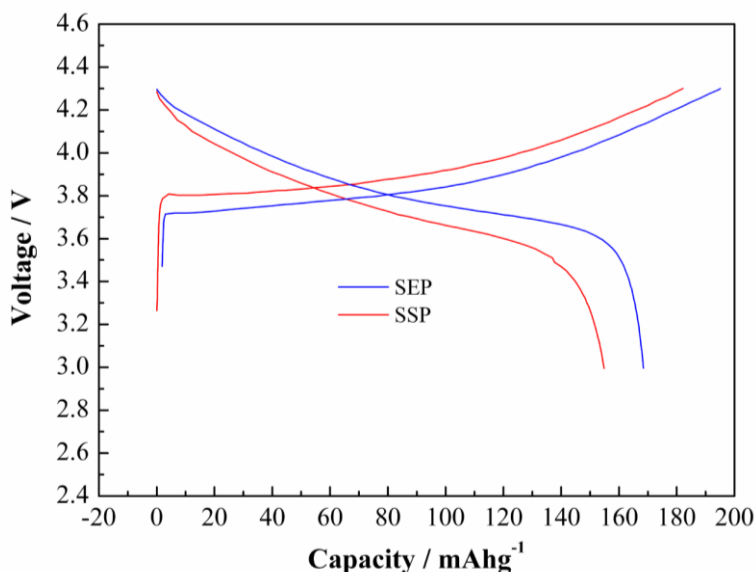
Figure 6. Initial charge-discharge curves of the samples operated in the voltages range of 3 ~ 4.3 V under a current density 20 mAg^{-1}.
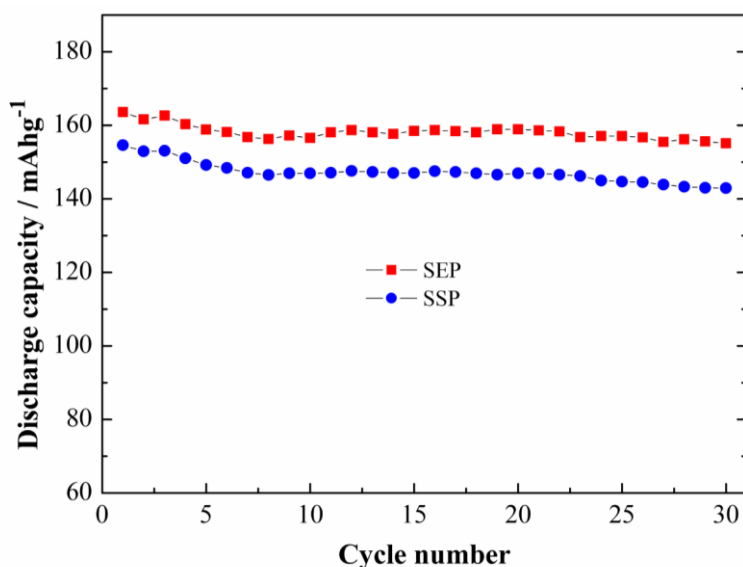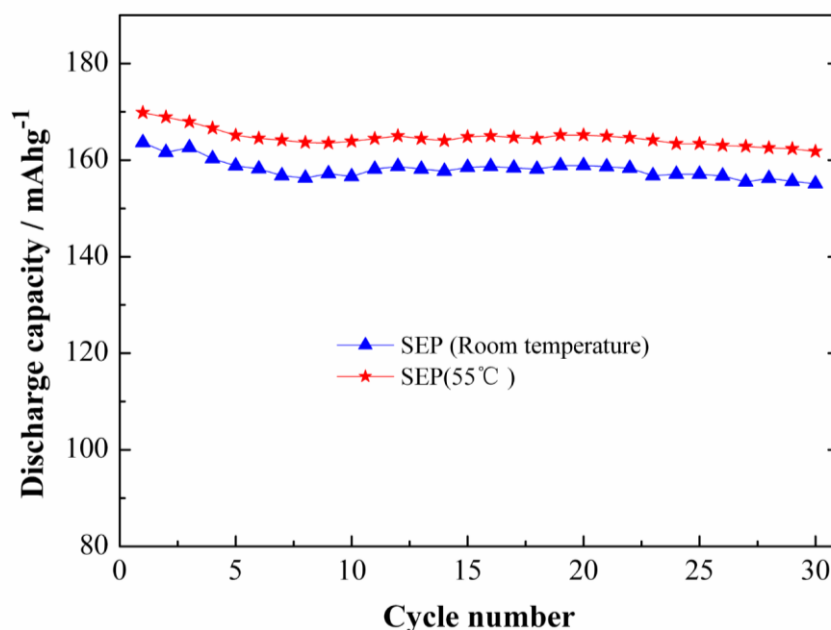

Figure 7. Specific discharge capacity as a function of cycle number for the samples operated in the voltage range of 3 ~ 4.3 V under a current density 20 mAg^{-1}.

From Figure 7, the two samples have excellent cyclic performances. The reversible capacities after 30 cycles are 159.7 mAhg^{-1} (94.8% of the initial discharge capacity) and 142.9 mAhg^{-1} (92.3% of the initial discharge capacity) for SEP and SSP, respectively. The higher discharge capacity of SEP, when compared to that of SSP, is caused by shorter diffusion length resulting from submicron-sized

particles. The particle size plays an important role on the lithium storage performance. The reduced dimension of the particles significantly increases the lithium insertion and deinsertion due to short diffusion length for lithium-ion transport within the particles. At the same time, an increased surface area with a smaller particle size results in increased side reactions with the electrolyte and thus forming thicker surface film (solid electrolyte interface, SEI). The thicker surface film would interfere badly with electrical contact between the particles during cycling and thus increasing capacity fading [23]. However, From Figure 7 the SEP still has an excellent cyclic performance although holding a smaller particle size compared to the SSP, which indicates that the cycling performance of the SEP is affected not only by the particle size but the structural integrity. These are consistent with the analytical XRD results. The obtained results thus strongly support that the solvent evaporation method is an effective method to prepare cathode material with higher capacity and cycling performance.


Figure 8. Specific discharge capacity as a function of cycle number for SEP operated at different temperatures in the voltage range of 3 ~ 4.3 V under a current density 20 mAg^{-1}.

In order to further investigate the electrochemical performances of SEP, we carried out the elevated temperature test and the rate capability experiments here. Figure 8 also gives the cycling stability of this material at 55 °C between 3.0 and 4.3 V at a current density of 20 mAg^{-1} (0.1C). It could be seen that a higher initial discharge capacity of 174.9 mAhg^{-1} may be obtained and after 30 cycles the discharge capacity is maintained 166.7 mAhg^{-1} (95.2% of the initial discharge capacity), which is slightly superior to the cycling property at room temperature.

Nazar et al. [24] have proved that the initial $R\bar{3}m$ phase is maintained up to the extraction of 0.7 ~ 0.75 Li. Additional extraction of Li results in the appearance of the $P\bar{3}m1$ phase, which leads to an increase in the irreversibility and rapid capacity fading. To avoid the appearance of the $P\bar{3}m1$ phase, the optimum upper cutoff voltage is 4.6V. Therefore, 4.6V is confirmed as an upper cutoff voltage in

our next experiments. Figure 9 shows the rate capability results of SEP at various current densities in the voltage range of 2.7 ~ 4.6V.
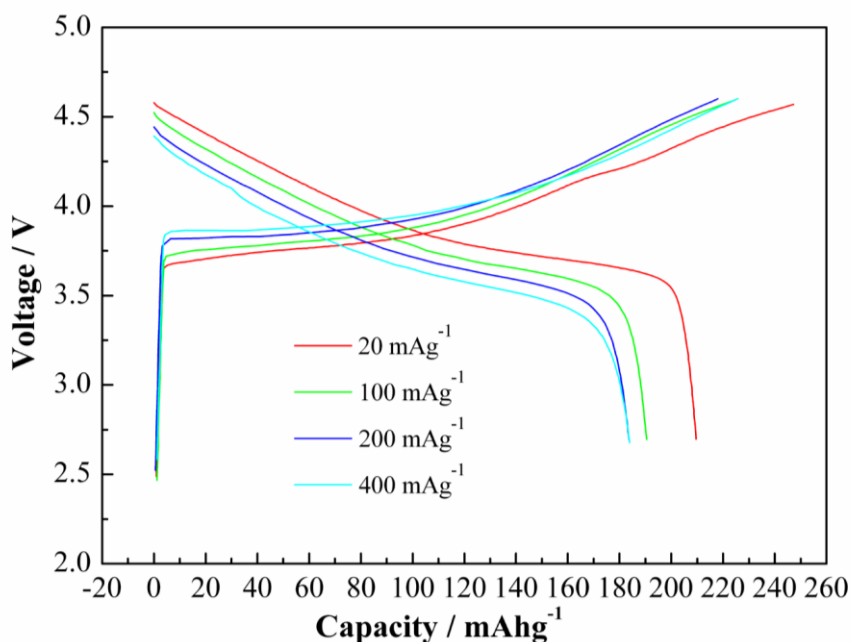
Figure 9. Initial charge-discharge curves of SEP operated in the voltages range of 2.7 ~ 4.6 V at different current densities.

At current densities of 20 mAg^{-1} (0.1C), 100 mAg^{-1} (0.5C), 200 mAg^{-1} (1C) and 400 mAg^{-1} (2C), the delivered initial discharge capacities of Li[Ni$_{1/3}$Co$_{1/3}$Mn$_{1/3}$]O$_2$ electrode are 209.6, 190.5, 183.7, and 182.6 $mAhg^{-1}$, respectively, which decrease with increasing current density. Compared to the discharge capacities in the voltage ranges of 3.0 ~ 4.3V and 2.7 ~ 4.6V at same current density of 20 mAg^{-1} (0.1C), it is obvious that the discharge capacities can be increased by enlarging the voltage range. We could also find from Figure 9 that the electrode shows a higher polarization at a bigger current density than that at a less current density.

Figure 10 presents the electrode cyclic performances at various current densities. It is clear that the electrodes still display better cycling stability even at higher voltage limit and bigger current densities. To our interest, at bigger current densities from 200 to 400 mAg^{-1}, the discharge capacities have no obvious decrease and keep similar cyclic performances. As well known, when voltage is higher (> 4.3V) for LiCoO$_2$ material, Co dissolution from LiCoO$_2$ has a detrimental effect on its electrochemical performances. The stable cyclability at higher voltage limit and bigger current densities in Figure 10 suggests that Co dissolution could be greatly suppressed by the formation of homogeneous Li[Ni$_{1/3}$Co$_{1/3}$Mn$_{1/3}$]O$_2$. Therefore, Li[Ni$_{1/3}$Co$_{1/3}$Mn$_{1/3}$]O$_2$ material is promising and superior to LiCoO$_2$.
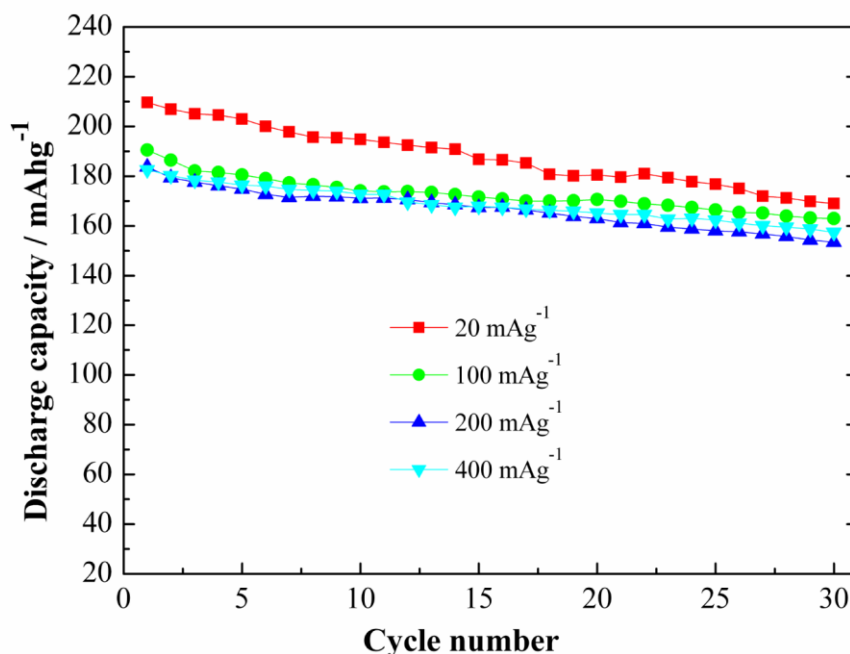
Figure 10. Specific discharge capacity as a function of cycle number for SEP operated in the voltages range of 2.7 ~ 4.6 V at different current densities.

4. CONCLUSIONS

Submicron-sized Li[Ni$_{1/3}$Co$_{1/3}$Mn$_{1/3}$]O$_2$ compound prepared by a solvent evaporation method holds different morphology, microstructure and electrochemical characteristics compared with that synthesized via a solid state. The electrochemical tests show that submicron-sized Li[Ni$_{1/3}$Co$_{1/3}$Mn$_{1/3}$]O$_2$ holds the higher initial discharge capacities of 168.5 mAhg^{-1} (3 ~ 4.3 V, 20 mAg^{-1}) and 209.6 mAhg^{-1} (2.7 ~ 4.6 V, 20 mAg^{-1}). Meanwhile, It also delivers an initial discharge capacity of 182.6 mAhg^{-1} even at higher voltage limit (4.6 V) and bigger current density (400 mAg^{-1}), and the capacity retention is above 86% at the 30th cycle. These results indicate that when preparing high-performance cathode material, the solvent evaporation method is both simple and efficient.

References

1. I.B. Weinstock, *J. Power Sources*, 110 (11) (2002) 471.
2. R. Santhanam and B. Rambabu, *Int. J. Electrochem. Sci*., 4 (2009) 1770.
3. K. Amine, C.H. Chen, J. Liu, M. Hammond, A. Jansen, D. Dees, I. Bloom, D. Vissers and G. Henriksen, *J. Power Sources*, 97–98 (2001) 684.

4. A.M. Andersson, D.P. Abraham, R. Haasch, S. MacLaren, J. Liu and K. Amine, *J. Electrochem. Soc.*, 149 (2002) A1358.
5. D. Ra and K. Hana, *J. Power Sources*, 163 (2006) 284.
6. T. Ohzuku and Y. Makimura, *Chem. Lett.*, 7 (2001) 642.
7. K.M. Shaju, G.V. Subba Rao and B.V.R. Chowdari, *Electrochim. Acta*, 48 (2002) 145.
8. D.C. Li, T. Muta, L.Q Zhang, M. Yoshio and H. Noguchi, *J. Power Sources*, 132 (2004) 150.
9. H. Ren, Y. Wang, D. Li, L. Ren, Z. Peng and Y. Zhou, *J. Power Sources*, 178 (2008) 439.
10. B. Jung, I. Jeong, K. Han, Y. Lee, D. Kim, J. Choo, M. Kim, K. Ryu, Y. Park, E. Kang and J. Jeong, Meeting Abstract of 1st International Conference on Polymer Batteries and Fuel Cell, Tu-072.
11. K.M. Shaju and P.G. Bruce, *Adv. Mater.*, 18 (2006) 2330.
12. T. Nukuda, T. Inamasu, A. Fujii, D. Endo, H. Nakagawa, S. Kozono, T. Iguchi, J. Kuratomi, K. Kohno, S. Izuchi and M. Oshitani, *J. Power Sources*, 146 (2005) 611.
13. Z. Wang, Y. Sun, L. Chen and X. Huang, *J. Electrochem. Soc.*, 151 (2004) A914.
14. S. Patoux and M.M. Doeff, *Electrochem. Commun.*, 6 (2004) 767.
15. J. Choi and A. Manthiram, *Electrochem. Solid-State Lett.*, 7 (2004) A365.
16. J. RodriguezCarvajal, *Physica B*, 192 (1993) 55.
17. J.M. Kim and H.T. Chung, *Electrochim. Acta*, 49 (2004) 937
18. M.H. Lee, Y.J. Kang, S.T. Myung and Y.K. Sun, *Electrochim. Acta*, 50 (2004) 939.
19. J.R. Dahn, U. Von Sacken and C.A. Michal, *Solid State Ionics*, 44 (1990) 87.
20. P.Y. Liao, J.G. Duh and S.R. Sheen, *J. Electrochem. Soc.*, 152 (2005) A1695.
21. B.J. Hwang, R. Santhanam and C.H. Chen, *J. Power Sources*, 114 (2003) 244.
22. Y.S. He, Z.F. Ma, X.Z. Liao and Y. J, *J. Power Sources*, 163 (2007) 1053.
23. R. Santhanam and B. Rambabu, *J. Power Sources*, 195 (2010) 4313.
24. S.C. Yin, Y.H. Rho, I. Swainson and L. F. Nazar, *Chem. Mater.*, 18 (2006) 1901.